Full length article

Strontium-driven physiological to pathological transition of bone-like architecture: A dose-dependent investigation

Camila Bussola Tovani [a,b], Thibaut Divoux [c], Sébastien Manneville [c], Thierry Azaïs [a], Guillaume Laurent [a], Marta de Frutos [d], Alexandre Gloter [d], Pietro Ciancaglini [b], Ana P. Ramos [b], Nadine Nassif [a,*]

[a] Laboratoire Chimie de la Matière Condensée de Paris, CNRS, Sorbonne Université, Collège de France, LCMCP, F-75005 Paris, France
[b] Departamento de Química, Faculdade de Filosofia, Ciências e Letras de Ribeirão Preto, Universidade de São Paulo, Ribeirão Preto, SP, Brazil
[c] Laboratoire de Physique, ENSL, CNRS, F-69342 Lyon, France
[d] Laboratoire de Physique des Solides (LPS), CNRS, Université Paris Saclay, F-91405 Orsay, France

A R T I C L E   I N F O

A B S T R A C T

Whilst strontium (Sr^{2+}) is widely investigated for treating osteoporosis, it is also related to mineralization disorders such as rickets and osteomalacia. In order to clarify the physiological and pathological effects of Sr^{2+} on bone biomineralization , we performed a dose-dependent investigation in bone components using a 3D scaffold that displays the hallmark features of bone tissue in terms of composition (osteoblast, collagen, carbonated apatite) and architecture (mineralized collagen fibrils hierarchically assembled into a twisted plywood geometry). As the level of Sr^{2+} is increased from physiological-like to excess, both the mineral and the collagen fibrils assembly are destabilized, leading to a drop in the Young modulus, with strong implications on pre-osteoblastic cell proliferation. Furthermore, the microstructural and mechanical changes reported here correlate with that observed in bone-weakening disorders induced by Sr^{2+} accumulation, which may clarify the paradoxical effects of Sr^{2+} in bone mineralization. More generally, our results provide physicochemical insights into the possible effects of inorganic ions on the assembly of bone extracellular matrix and may contribute to the design of safer therapies for treating osteoporosis.

Statement of significance

Physiological-like (10% Sr^{2+}) and excess accumulation-like (50% Sr^{2+}) doses of Sr^{2+} are investigated in 3D biomimetic assemblies possessing the high degree of organization found in the extracellular of bone. Above the physiological dose, the organic and inorganic components of the bone-like scaffold are destabilized, resulting in impaired cellular activity, which correlates with bone-weakening disorders induced by Sr^{2+}.

1. Introduction

Strontium (Sr^{2+}) is naturally present in the human body as a trace element in mineralized tissues (bones and teeth) [1]. Over the past decades, the administration of Sr^{2+} has been described as beneficial as it can reestablish the imbalanced activity between osteoclasts (bone resorption cells) and osteoblasts (bone-forming cells), which is the primary cause of osteoporosis [2]. This has motivated the formulation of strontium ranelate, a drug with Sr^{2+} as the active component for treating and preventing osteoporosis, a major bone disease affecting hundreds of millions of elderly people worldwide [3]. Consequently, Sr^{2+}-based biomaterials and oral therapies have emerged over the last years as promising opportunities to treat this widespread bone disease [4,5]. However, paradoxically, clinical studies have reported a link between the high concentration of Sr^{2+} in bone and the development of disorders such as rickets and osteomalacia (also known as soft bones), which are characterized by abnormal mineralization of the extracellular matrix and accumulation of osteoid tissue [6–8]. The main clinical consequences of bone weakening caused by these disorders include skeletal deformities, poor growth, fractures, and severe pain [9,10]. This dichotomy poses clinical concerns for the

---

* Corresponding author.
  E-mail address: nadine.nassif@sorbonne-universite.fr (N. Nassif).

main target of osteoporosis treatments (*e.g.*, elderly people and postmenopausal women), where an imbalance between Sr^{2+} uptake and removal is reported due to a decreased renal function [11]. In addition, Sr^{2+} is heterogeneously distributed in bones of osteoporotic patients treated with strontium ranelate with a selective uptake in newly formed osteon, which suggests the involvement of Sr^{2+} at the early stages of bone formation [12,13].

In this context of biomineralization, *in vitro* models have shown that the structure of apatite, *e.g.,* the mineral phase of bone, is not altered at physiological-like concentrations of Sr^{2+}(i.e., 10%) [12], except for a slight increase in the lattice parameters [14–17]. Recently, we found that the bone-like apatite structure is disrupted in excess of Sr^{2+}, leading to the formation of a stable Sr^{2+}-rich amorphous calcium phosphate phase Sr(ACP) [17]. Although the effects of Sr^{2+} have been widely investigated, the studies mainly focus on a physiological context as well as on the mineral component precluding the understanding at the higher level of bone hierarchy) [18]. Therefore, there is a real benefit in studying the dose/effect relationship of Sr^{2+} with models that comprise the hybrid organic/inorganic structure of the tissue.

Here, we investigate physiological-like (10% Sr^{2+}) and excess accumulation-like (50% Sr^{2+}) amounts of Sr^{2+} in 3D biomimetic assemblies possessing the main structural hallmarks of bone tissue, *i.e.,* the plywood motif of collagen fibrils and carbonated apatite nanoparticles [19]. While 10% Sr^{2+} does not induce any structural modification, an excess of Sr^{2+} leads to the destabilization of both the fibrillar self-assembly of collagen and the apatite structure. Concomitantly, the local mechanical properties of the 3D scaffolds show a strong softening in the presence of an excess of Sr^{2+}, *i.e.,* the Young modulus drops by a factor of two compared to physiological-like conditions. In the pathological-like scenario, micrometric particles of Sr^{2+}-rich amorphous calcium phosphate Sr(ACP) are formed, destabilizing the typical three-dimensional architecture found in bone. We further show that such destabilization of the matrix microstructure leads to an impaired adhesion of preosteoblastic cells. Our observations correlate with the increased osteoid reported for Sr^{2+}-driven bone disorders [20–22] and contribute to clarifying the ambiguous role of this element on bone mineralization. Such results may have broad implications for the safer design of bone regenerative therapies. From a material perspective, this investigation highlights the intriguing destabilization of the collagen network by amorphous calcium phosphate particles, which are regarded as the precursor of bone minerals [23,24].

2. Experimental procedure

2.1. Collagen extraction

Type I collagen monomers were extracted from rat tail tendons following a classical procedure [25]. Briefly, fresh tendons were washed with phosphate-buffered saline (0.01 mol L^{-1} PBS) solution to remove traces of cells and blood and then solubilized in 0.5 mol L^{-1} acetic acid. The crude solution was centrifuged, and the supernatant was selectively precipitated with 0.7 mol L^{-1} NaCl. Precipitated type I collagen was solubilized in 0.5 mol L^{-1} acetic acid and desalted by dialysis against 0.5 mol L^{-1} acetic acid. The collagen concentration in the stock solution was determined by hydroxyproline titration [26] and then adjusted to 3 mg mL^{-1}.

2.2. Preparation of mineralized collagen matrices at different concentrations of Sr^{2+}

Disk-shaped collagen matrices with a thickness of ~3 mm and a width of ~12 mm were prepared by combining continuous injection and reverse dialysis [19]. 15 mL of 1 mg mL^{-1} collagen acidic solution was mixed with SrCl$_2$/CaCl$_2$/NaH$_2$PO$_4$/NaHCO$_3$ acidic solution (0.5 mol L^{-1} acetic acid). Mixtures containing different Sr^{2+} molar percentages (namely 0, 10, and 50%) in relation to the total number of moles of divalent cations ($Ca^{2+} + Sr^{2+}$) were prepared. Throughout the article, we refer to the samples prepared in the absence of Sr^{2+} as Coll-CaP-0%Sr^{2+} and those prepared in the presence of 10% Sr^{2+} and 50% Sr^{2+} as Coll-CaP-10%Sr^{2+} and Coll-CaP-50%Sr^{2+}, respectively. The (Ca + Sr)/(P + C) ratio was kept constant and equal to 1.67, and the pH was ~3.5. The final concentrations of the salt precursors were CaCl$_2$ (46.1 mmol L^{-1}), SrCl$_2$ (46.1 mmol L^{-1}), NaH$_2$PO$_4$ (13.8 mmol L^{-1}), and NaHCO$_3$ (13.8 mmol L^{-1}). The collagen/salts mixtures were continuously injected in a closed dialysis mold. The bottom of the chamber was a dialysis membrane with a molecular weight cut-off of 12–14 kDa. A reverse dialysis process was performed against polyethylene glycol (PEG, 35 kDa, Fluka) dissolved in 5 mol L^{-1} acetic acid up to 300 mg ml^{-1}. The ionic precursors of apatite were dissolved in both the collagen and the PEG solution. The global ionic strength (165.9 mmol L^{-1}) was kept constant throughout the process and was close to that described in physiological conditions. After complete collagen injection, dialysis was continued for 4 days in order to obtain the same concentration over the sample. Then, by increasing the pH in the range of 9 to 10 by NH$_3$ diffusion for 4 days, the precipitation of collagen fibrils and minerals was simultaneously triggered. Finally, the matrices were removed from the dialysis chamber and continuously washed with PBS (pH=7.4) in order to reach neutral pH. All experiments were carried out at a controlled temperature of 19 $\pm$ 2 °C in order to prevent collagen denaturation, and sterility conditions were applied throughout the procedure. The concentration of type I collagen in the matrices was assessed by hydroxyproline titration [26]. Control experiments were performed by precipitation of calcium/strontium phosphate particles in the absence of collagen. For this purpose, the mixtures containing different Sr^{2+} molar percentages (namely 0, 10, and 50%) in relation to the total number of moles of divalent cations ($Ca^{2+} + Sr^{2+}$) were exposed to NH$_3$ vapor for 4 days. Throughout the article, we refer to the samples prepared in the absence of collagen as CaP-0%Sr^{2+}, CaP-10%Sr^{2+}, and CaP-50%Sr^{2+}.

2.3. Bone sampling

2.3.1. Fresh bone

Bone was extracted (about 1 cm^3) from the proximal part of the diaphysis and distal epiphysis of humerus and femur from 2-year-old healthy French sheep with a drill following the classical procedure described by Nuss et al [27]. The bone fragments were kept hydrated in phosphate buffer solution (0.01 mol L^{-1} PBS) until characterization (up to 1 hour) then directly prepared following the sample preparation for scanning electron microscopy (SEM) and transmission electron microscopy (TEM) observations or directly inserted in a rotor for the solid-state nuclear magnetic resonance (ssNMR). The study was reviewed and approved by the IMM Recherche's Institutional Animal Care and Use Committee (IACUC) prior to the initiation of this study. The Animal Care and Use Committee of IMMR is registered at the CNREEA under the Ethics Committee n°37. The animal research center (IMM-Recherche) received an agreement (n°75-14-01) by the "Direction Départementale de la Protection des Populations". The studies were also performed in compliance with the Principles of Laboratory Animal Care, formulated by the National Society for Medical Research, and the Guide for the Care and Use of Laboratory Animals by the Institute of Laboratory Animal Resources (published by the National Academy Press, Washington, D.C, 1996), as amended by the Animal Welfare Act of 1970 (P.L 91-579) and the 1976 amendments to the Animal Welfare were followed.

2.4. Sample characterization

2.4.1. Histological preparation for optical microscopy

Samples were fixed in 4% paraformaldehyde in PBS for 24 h, dehydrated through successive ethanol baths (v/v 70%-24h, 95%-3h, and 100%-3h) followed by 3 days bath in butan-1-ol and embedded in paraffin. Thick sections of 7 μm, transverse to the sample surface, were stained with picrosirius. This red staining is used to probe collagen in normal and pathological tissues.

2.4.2. Light microscopy under polarized light

Histological sections were observed with a Zeiss AxioImager A2 POL microscope equipped with crossed polarizers and an AxioCam CCD camera.

2.4.3. Scanning and transmission electron microscopy

For scanning electron microscopy (SEM) analysis, the matrices and bone sample were fixed in 3.6% glutaraldehyde in PBS (v/v) and dehydrated through successive ethanol baths (v/v 30%, 50%, 70%, 80%, 90%, 95%, and 100%) for supercritical CO_2 drying performed on a CPD 300 check. Samples coated with gold (10 nm layer) were studied by SEM using a Hitachi model S-3400N SEM at an accelerating voltage of 9 kV. For transmission electron microscopy (TEM) observations, the synthetic and biological samples were fixed with glutaraldehyde, dehydrated through successive ethanol baths (v/v 70%-24 h, 95%-3 h, and 100%-3 h), and embedded in Araldite. Ultrathin Araldite sections (60 or 70 nm) were contrasted with uranyl acetate and analyzed with a FEI TECMAI G2 Spirit Twin electron microscope operating at 120 kV.

2.4.5. Thermogravimetric analysis (TGA)

Experiments were performed on a thermo-microbalance instrument (TG 209 F1, Netzsch GmbH, Selb, Germany) with the air-dried sample. The measurement was performed from 20 °C to 800 °C in an air atmosphere with a heating rate of 10 °C min^{-1}. The final mass of the components was calculated by excluding the mass of free water. For this purpose, 100% weight of each sample was set at T = 120 °C.

2.4.6. Solid-state nuclear magnetic resonance (ssNMR)

Two dimensional ^{1}H-^{31}P Cross Polarization Magic Angle Spinning (CPMAS) heteronuclear correlation experiments (^{1}H-^{31}P Het-Cor) were performed on an AVANCE 300 Bruker spectrometer operating at $\nu(^1H) = 300.13$ MHz and $\nu(^{31}P) = 121.50$ MHz using contact time t$_{CP}$ = 1 ms. The samples were packed in 4 mm zirconia rotors that were spun at a MAS frequency of 8 kHz. The chemical shifts were referenced to H_3PO_4 85%wt for ^{31}P (0 ppm) and adamantane for ^{1}H (0 ppm).

2.4.7. Nanoindentation for measuring local elastic properties

The local mechanical properties of mineralized collagen matrices were determined by nanoindentation at room temperature (22°C). Experiments were performed with a nanoindenter (PIUMA, Optics 11) equipped with a spherical probe made of glass (radius R=56.5 μm) and attached to a cantilever of calibrated stiffness (k=0.170 N/m). The test consisted of depth-controlled indentations of maximum depth set to 4 μm (yielding a typical contact radius between the sphere and the sample of about 10-15 μm) and performed over a square grid composed of 10 × 10=100 indentations, each spaced by 50 μm, hence covering a region of interest of size 500 μm x 500 μm. Indentations were performed following a symmetric displacement profile consisting of a loading phase (2 s), a constant force (so-called creep) phase (1 s), followed by unloading (2 s). Typical forces reached at the end of the loading phase were about 0.5 μN. Finally, for each indentation, the force-depth curve was fitted by a Hertzian contact model, yielding the effective

Young modulus E_{eff} at the locus of the indent. The Young modulus E was then computed following $E = E_{eff}(1 - \nu^2)$, assuming a Poisson ratio ν of 0.5 for all samples.

2.4.8. Zeta potential (ζ) measurements

The surface charge of the scaffolds was investigated by ζ. The samples were prepared by cryogenic-grinding, and the resulting powders were dispersed in α-MEM supplemented with 10% fetal bovine serum. The measurements were carried out using a Malvern Zetasizer Nano ZS90.

2.5. Cell culture experiments

2.5.1. Cell viability –MTT
(3-4,5-dimethylthiazol-2,5-diphenyltetrazolium bromide) assay

Osteoblastic lineage cells MC3T3-E1 (American Type Culture Collection-ATCCt) were cultured in a minimum essential medium (α-MEM, Gibco) supplemented with 10% fetal bovine serum and 1% (v/v) penicillin/streptomycin. The osteogenic medium was achieved by the addition of 50 mg/mL ascorbic acid and 10 mM beta-glycerophosphate. First, the collagen matrices were plated on the 24-well plates for 24 h to equilibrate with the culture medium. Then, the cells were seeded on the matrices at the density of 2×10^4 cells per well and incubated in air at 37 °C with 5% CO_2. The culture medium was changed every two days. Cell viability was determined by the classic MTT assay after 7 and 14 days of culture using the protocol described by Mosmann [28]. Cell viability was expressed as the percentage of the average of three experiments as compared to the control (Ct) cultured on polystyrene wells for each day of culture (100%).

As a control, the cells were first seeded on 24-well plates at the density of 2.10^4 cells per well and incubated in air at 37 °C and 5% CO_2 with the CaP-0%Sr^{2+}, CaP-10%Sr^{2+}, and CaP-50%Sr^{2+} particles formed in the absence of collagen. For this purpose, the plated cells were allowed to attach to the polystyrene well bottoms for 24h, followed by the replacement of the medium by a suspension of the calcium/strontium phosphate particles at 1 μg mL^{-1} in the culture medium. The culture medium was changed every two days keeping constant the concentration of the particles. Cell viability was determined by MTT assay after 7 and 14 days of culture. Cell viability was expressed as the percentage of the average of three experiments as compared to the control (Ct) without treatment for each day of culture (100%).

2.5.2. Alkaline phosphatase (ALP) activity

ALP activity was determined by quantifying the hydrolysis of the substrate p- nitrophenyl phosphate (PNPP) in the plasma membrane fraction extracted from cells after 7 and 14 days of culture, according to the protocol described elsewhere [29]. The enzymatic activity was normalized by the total protein content which was estimated in the presence of 2% (w/v) sodium dodecyl sulfate using bovine serum albumin as standard.

2.5.3. Cell morphology

The cells cultured on the collagen matrices were fixed in 1.5% glutaraldehyde (v/v) at 4 °C for 12 h, dehydrated through a series of ethanol concentrations (v/v, 20, 50, 70, 80, 90, and 100%) then dried using supercritical CO_2 conditions and contrasted with osmium. After gold coating, the samples were observed on a Zeiss-EVO 50 SEM microscope under 20 kV accelerating voltage.

2.5.4. Statistical analyses

For the studies of cell viability and ALP activity, multiple statistical comparisons were performed by one-way ANOVA in relation to the control, $**p < 0.01$. Results represent the mean values $\pm$ standard deviation for triplicate determination for one experiment.

3. Results and discussion

Two types of scaffolds were prepared in the presence of 10% Sr^{2+} and 50% Sr^{2+} tending to mimic the two main scenarios described for Sr^{2+} incorporation in bone: (i) physiological (Coll-CaP-10%Sr^{2+} scaffold) and (ii) pathological (Coll-CaP-50%Sr^{2+} scaffold). In addition, control experiments were performed both by forming the bone-like scaffold in the absence of strontium (Coll-CaP-0%Sr^{2+} scaffold) and by precipitating mineral in the absence of collagen (CaP-0%Sr^{2+}, CaP-10%Sr^{2+}, and CaP-50%Sr^{2+}). The different conditions are summarized in **Table a.**

3.1. The Impact of Sr^{2+} on Collagen Fibrils Mineralization

We first characterized the mineral phase formed in the collagen scaffolds at the hydrated state using ssNMR (Fig. 1). From 2D ^1H-^{31}P HetCor experiments, we observe that the Coll-CaP-10%Sr^{2+} scaffold exhibits a ^{31}P NMR signature composed of two distinct resonances assigned to the coexistence of different domains in the mineral, which is the spectroscopic fingerprint of bone apatite [30]. (Fig. 1b *versus* Fig. 1c): a crystalline core (sharp signal at $\delta(^{31}P) \approx$ 2.8 ppm correlating with hydroxyl ions at $\delta(^1H) = 0$), and a disordered surface layer (broader signal at $\delta(^{31}P) \approx$ 3.2 ppm correlating with water molecules at $\delta(^1H) = 4.8$ ppm). However, the spectrum for Coll-CaP-10%Sr^{2+} exhibits larger linewidths and a subtle shift compared to bone and Coll-CaP-0%Sr^{2+} (Fig. S1) reflecting a higher local disorder in the crystalline core. This difference is ascribed to the replacement of Ca^{2+} by Sr^{2+} in the apatite structure, as previously described for both biomimetic apatite formed in the absence of collagen [16,17], and bone mineral [14,31,32]. In contrast, the ^{31}P signal from the 2D ^1H-^{31}P HetCor spectrum for Coll-CaP-50%Sr^{2+} is dominated by a broad linewidth together with a weak signal from apatite (Fig. 1d). The similarity between the ^{31}P projection of Coll-CaP-50%Sr^{2+} at $\delta(^1H) = 5.0$ ppm and the quantitative ^{31}P spectra of CaP-50%Sr^{2+} show that the mineral formed in the scaffold is majoritarily Sr(ACP) (Fig. 1e). This result reveals that the presence of collagen does not preclude the destabilization of apatite induced by high-dose of Sr^{2+}.

After investigating the atomic environment of minerals, TEM observations were performed to characterize their morphology, size, and spatial distribution. Nanometric apatite platelets are formed at 10% Sr^{2+} (Fig. 1f) as classically observed in bone (Fig. 1g and Fig. S2a) and in the biomimetic Coll-CaP-0%Sr^{2+} scaffold (Fig. S1b) [19,33]. Overall, a comparison of the minerals shows that Sr^{2+} at a physiological-like concentration does not interfere with the ability of collagen to define the structure and morphology of apatite. In contrast, non-physiological dense rounded particles ($\sim$ 500 nm) are observed within the Coll-CaP-50%Sr^{2+} scaffold (Fig. 1h and Fig. S2b). In line with the NMR results, these particles resemble Sr(ACP) formed in the absence of collagen (Fig. S3).

3.2. The Impact of Sr^{2+} on the Bone-like suprafibrillar assembly of collagen (plywood pattern)

We next investigated how the formation of rounded Sr(ACP) *versus* Sr^{2+}-substituted apatite platelets influences the supramolecular assembly of collagen fibrils. It should be noted that previous studies have also investigated the mineralization of collagen fibrils in the presence of Sr^{2+} [34,35]. However, the impact of this element was never investigated on 3D biomimetic assemblies. To this aim, additional TEM investigations were performed on stained sections (Fig. 2). Cross-striated fibrils are still observed at low concentrations of Sr^{2+} (Fig. 2a, Coll-CaP-0%Sr^{2+} and Fig. 2b Coll-CaP-10%Sr^{2+}) showing that Sr^{2+} does not affect the self-assembly and packing of collagen molecules. In contrast, no evident fibrillar organization was observed in the presence of Sr(ACP) (Fig. 2c, Coll-

CaP-50%Sr^{2+}), suggesting a destabilization of the collagen assembly at Sr^{2+} excess. To investigate whether this effect also occurs at larger scales, the scaffolds were then transversally fractured, and both the surface (Fig. 2d-f) and the bulk (Fig. 2g-i) fibrils were observed by SEM. Consistent with TEM images, it is also challenging to discriminate differences in the 3D architecture of collagen fibrils in Coll-CaP-0%Sr^{2+} and Coll-CaP-10%Sr^{2+} as both scaffolds display a tissue-like appearance with closely packed fibrils at the surface and a cholesteric twisted plywood geometry in bulk, similar to the pattern observed in bone [36] (Fig. S4a and Fig. S4b, respectively). Conversely, the Coll-CaP-50%Sr^{2+} scaffold displays a random fibril-like array at the surface and in bulk with the presence of macropores (arrows in Fig. 2f) reflecting a higher interfibrillar space. The cholesteric geometry of collagen fibrils in Coll-CaP-0%Sr^{2+} (Fig. 3a-a') and Coll-CaP-10%Sr^{2+} (Fig. 3b-b') is further evidenced by polarized light microscopy images where a strong optical birefringence is observed throughout the thin section. After a 45° rotation of the polarizers, extinction of light occurs in areas where the collagen fibrils lie parallel to the direction of the polarizers indicating their cholesteric organization (Fig. 3a' and Fig. 3b'). Interestingly, Coll-CaP-50%Sr^{2+} also exhibits a nematic birefringent texture which indicates that isotropic and anisotropic domains exist within the scaffold. Nevertheless, cholesteric domains are never observed which also attests to the destabilization of collagen assembly at large scales (Fig. 3c-c'). Overall, our observations fit into the two major landscapes of Sr^{2+} incorporation in bone: (i) the pathological accumulation, where disorder in the extracellular matrix is observed, and (ii) therapeutic administration, where no obvious changes are detected in the tissue microstructure.

Next, we determined the microscale mechanical properties of the different scaffolds with various contents in Sr^{2+}, in order to quantify the impact of the change in microstructure described above on the scaffold elasticity.

3.3. Impact of Sr^{2+} on the local mechanical properties of collagen scaffold

Nanoindentation experiments allow measuring the local mechanical properties of the collagen scaffold on a region of interest corresponding to a square grid of size 500 µm. Each indentation at the node of the grid provides a local elastic modulus averaged over a volume set by the contact area between the spherical indenter and the sample, which radius is about 10-15 µm for an indentation depth of 4 µm. The size of the indentations was chosen to investigate the mechanical behavior of the scaffolds at the scale of one cell.

First, we observe that the Young moduli computed from the 100 indentations show a Poisson distribution for the two samples with the lowest content in Sr^{2+}, *i.e.*, Coll-CaP-0%Sr^{2+} and Coll-CaP-10%. In contrast, the Young moduli for Coll-CaP-50%Sr^{2+} follow a Gaussian distribution (Fig. 4d). Moreover, samples Coll-CaP-0%Sr^{2+} and Coll-CaP-10% Sr^{2+} display comparable average values of about 8 kPa, whereas Coll-CaP-50%Sr^{2+} shows much weaker elastic properties characterized by an average Young modulus of about 4 kPa (Fig. 4e). Such a drop in elasticity for the highest content in Sr^{2+} correlates well with the Sr^{2+}-induced destabilization of the collagen self-assembly and the presence of a porous-like microstructure in Coll-CaP-50%Sr^{2+} visible at the spatial scale of indentation.

Second, the indentation grid provides a spatially-resolved picture of the sample elastic properties in the region of interest, with a spatial resolution set by the distance between two consecutive indents, here fixed to 50 µm. Representative elasticity maps are reported in Fig. 4a-c for the three types of collagen scaffolds. For samples Coll-CaP-0%Sr^{2+} and Coll-CaP-10%Sr^{2+}, we observe large-scale heterogeneities of size 200 µm, which might correspond to different arrangements of the fibrils at the sample surface. In con-

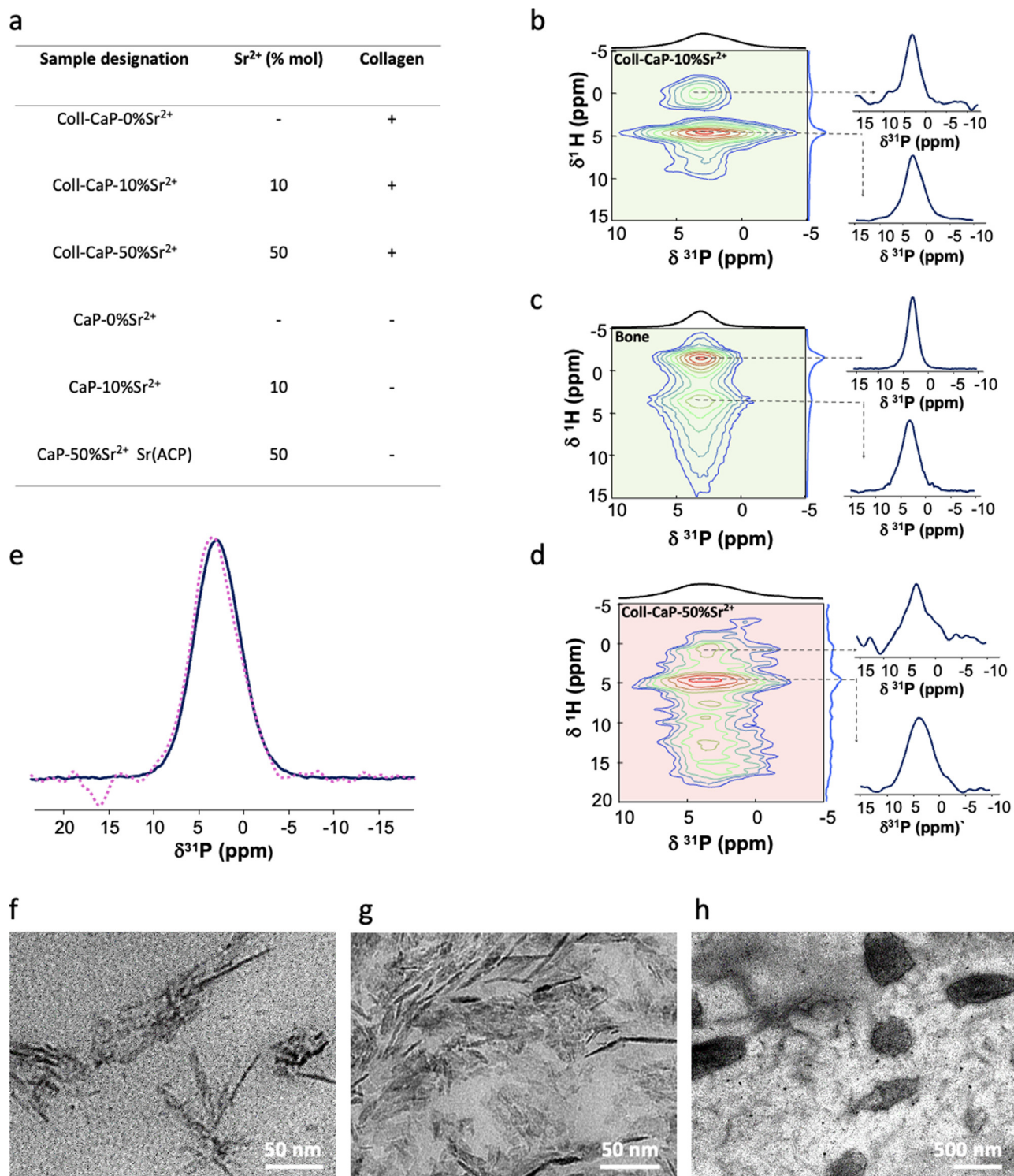**Fig. 1.** Effect of Sr^{2+} on bone-like apatite formed within collagen scaffold. Table (a). Summary of experimental conditions. ^{1}H-^{31}P HetCor spectra of (b) Coll-CaP-10%Sr^{2+}, (c) fresh bone and (d) Coll-CaP-50%Sr^{2+}. (e) Comparison of the ^{1}H-^{31}P HetCor extracted ^{31}P row at $\delta(^{1}H) = 5.0$ ppm of Coll-CaP-50%Sr^{2+} scaffold and the ^{31}P quantitative spectra of CaP-50%Sr^{2+} particles. TEM images of (f) Coll-CaP-10%Sr^{2+}, (g) bone mineral, and (h) Coll-CaP-50%Sr^{2+}.

trast, Coll-CaP-50%Sr^{2+} displays a more homogeneous distribution of the Young modulus at the spatial scale investigated, insensitive to the presence of the non-physiological 500 nm particles. Such a discrepancy is reflected in the relative standard deviation, i.e., the ratio of the standard deviation to the mean value, of the distributions shown in Fig. 4d, which reaches 53% and 66% for Coll-CaP-0%Sr^{2+} and Coll-CaP-10%Sr^{2+}, respectively, while it is only of

31% for Coll-CaP-50%Sr^{2+}. Furthermore, a paired-sample t-test performed on the Coll-CaP-0%Sr^{2+} and Coll-CaP-10%Sr^{2+} data yield a p-value of 0.068 (which increases up to 0.127 when a single outlier at more than 5 times the mean value in the 10%Sr^{2+} data is disregarded), which is large enough to consider that these data are statistically equivalent with the standard significance level of 0.05. By contrast, unsurprisingly, the same t-test performed either
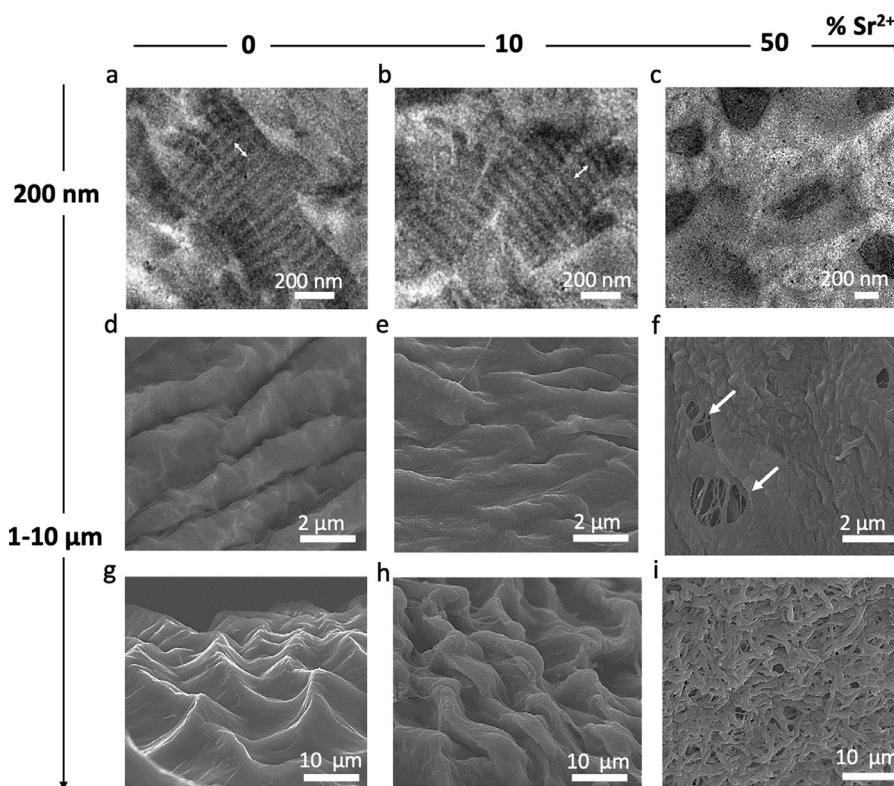
Fig. 2. Effect of Sr^{2+} concentration on supramolecular assembly of collagen fibrils. TEM images of (a) Coll-CaP-0%Sr^{2+}, (b) Coll-CaP-10%Sr^{2+}, and (c) Coll-CaP-50%Sr^{2+}. Double headed arrows in a and b denote the 67 nm periodicity. SEM images showing the surface of (d) Coll-CaP-0%Sr^{2+}, (e) Coll-CaP-10%Sr^{2+}, and (f) Coll-CaP-50%Sr^{2+}. SEM images showing the interior of fractured (g) Coll-CaP-0%Sr^{2+}, (h) Coll-CaP-10%Sr^{2+}, and (i) Coll-CaP-50%Sr^{2+}. The white arrows in (f) indicate the presence of pores in the scaffold.
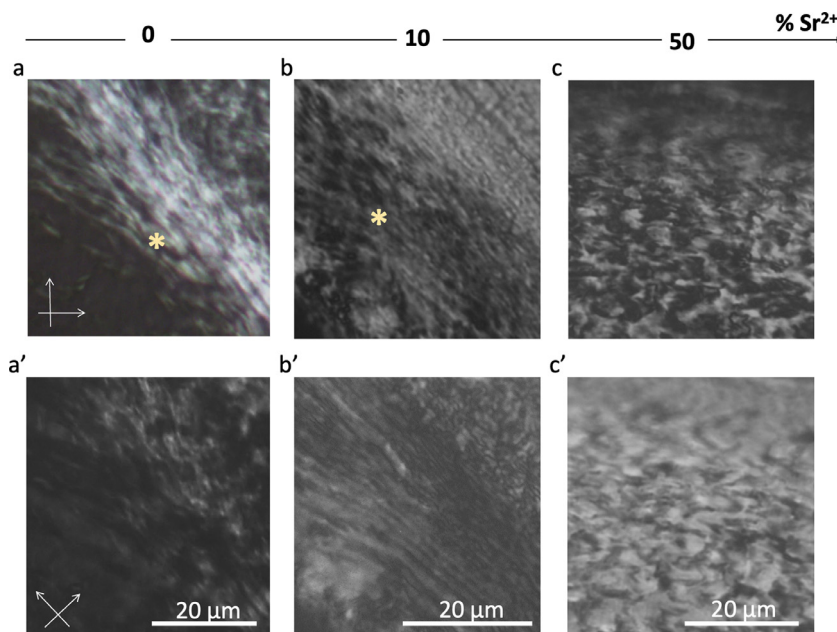

Fig. 3. Effect of Sr^{2+} concentration on the organization of collagen scaffold. Polarized light microscopy images of (a-a') Coll-CaP-0%Sr^{2+}, (b-b') Coll-CaP-10%Sr^{2+}, and (c-c') Coll-CaP-50%Sr^{2+}. The asterisk in (a) and (b) indicate the presence of cholesteric domains that turn bright after a 45° rotation of both polarizers [see arrows in (a) and (a')].

on the Coll-CaP-0%Sr^{2+} and Coll-CaP-50%Sr^{2+} data or on the Coll-CaP-10%Sr^{2+} and Coll-CaP-50%Sr^{2+} data yield vanishingly small p-values ($<10^{-11}$). Thus, mechanical measurements show that collagen scaffolds in excess of Sr^{2+} are significantly softer, and more homogeneous than samples with a low Sr^{2+} content. Although simultaneous structural and mechanical measurements, e.g., through atomic force microscopy, would be needed to fully corroborate the impact of the fibril arrangement and/or of the presence of non-physiological particles on the local Young modulus, our *in vitro* results agree with the so-called "soft bones disorder" reported *in vivo* [10]. Next, we investigated the impact of changes in the microstructural and mechanical properties of strontium-loaded scaffolds on bone forming cells.
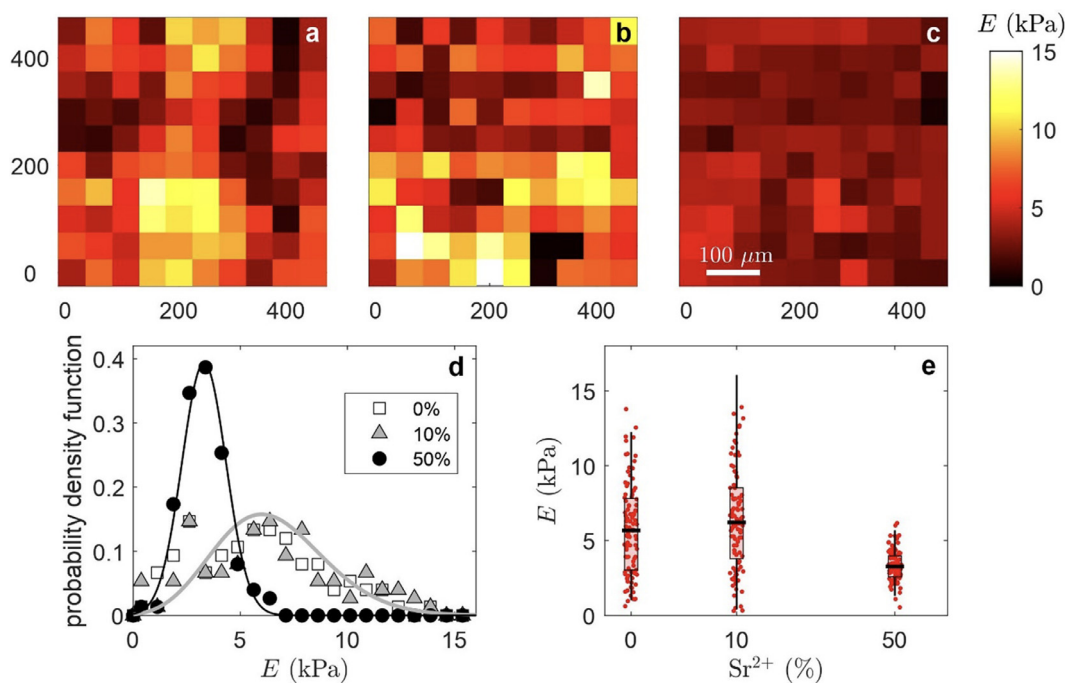
Fig. 4. Effect of Sr^{2+} on the mechanical properties of collagen scaffold. Elasticity map over a region of interest of 500 μm square for (a) Coll-CaP-0%Sr^{2+} (b) Coll-CaP-10%Sr^{2+}, and (c) Coll-CaP-50%Sr^{2+}. Colors code for the Young modulus E. The probability density function of E is shown in (d) for the three samples of interest; the gray (resp. black) curve shows the best fit of the data by a Poisson (resp. Gaussian) distribution. The same data are reported as a Raincloud plot [37] in (d). For each data set, raw values of E determined at distinct locations of the sample appear as dots, while the box represents one standard deviation above and below the mean, itself marked by a horizontal black dash.

3.4. Bone cells response on strontium-loaded scaffolds

Pre-osteoblasts were cultured for 7 days on Coll-CaP-0%Sr^{2+}, Coll-CaP-10%$Sr^{2+,}$ and Coll-CaP-50%Sr^{2+} scaffolds (Fig. 5a-c'). Cells grew flat on Coll-CaP-0%Sr^{2+} (Fig. 5a-a') and Coll-CaP-10%Sr^{2+} (Fig. 5 b-b') displaying elongated morphology, which suggests their strong anchoring and spreading on these matrices [38]. The cell elongation indicates that the anisotropic matrices provided cues to guide their unidirectional adhesion along the axis of the collagen fibrils [39,40]. The suitable interaction between the cells and these substrates is further shown by the presence of filopodia (arrows in Fig. 5a and Fig. 5b) contacting neighboring cells and extending along the matrices surface [41]. In contrast, the cells seeded on Coll-CaP-50%Sr^{2+} display a spherical morphology, which reflects their low affinity for the scaffold (Fig. 5c-c') [42]. After 7 and 14 days of culture, the viability of cells was maintained on Coll-CaP-0%Sr^{2+} and Coll-CaP-10%Sr^{2+} and decreased on Coll-CaP-50%Sr^{2+} (Fig. 5d), supporting SEM observations. The ALP activity, an early marker for osteoblasts differentiation, was also reduced for the cells cultured on Coll-CaP-50%Sr^{2+} suggesting that their evolution towards mature mineralizing osteoblasts was hindered as compared to the cells cultured on Coll-CaP-0%Sr^{2+} and Coll-CaP-10%Sr^{2+} scaffolds (Fig. 5e).

The impact of different mineralization degrees of the scaffolds on cells behavior is discarded here since their mineral content is in the same range as demonstrated by TGA (20% for Coll-CaP-0%Sr^{2+}, 18% for Coll-CaP-10%Sr^{2+} and 15% for Coll-CaP-50%Sr^2) (Fig. S5). Furthermore, we can also exclude the influence of charge since the scaffolds display similar global charge in the cell culture environment with a zeta potential $\zeta \approx$ -6 mV. Finally, the calcium phosphate particles formed without collagen (CaP-0%Sr^{2+}, CaP-10%$Sr^{2+,}$ and CaP-50%Sr^{2+}) did not display toxicity towards MC3T3-E1 (Fig. 5f), which is in agreement with previous studies [43]. These results emphasize the impact of the scaffold struc-

ture/property on the cell response. Indeed, local defects in the bone matrix lead to impaired osteoblasts migration and maturation, preventing mineralization from progressing normally, as described in several bone disorders [44,45]. Noticeably, while it is commonly reported that high Sr^{2+} concentration impairs cell viability [46], here we show the physicochemical interference of Sr^{2+} with the bone-like matrices comprising the destabilization of apatite and collagen network which extends to cells behavior. It should be noted that although osteoblasts are responsible for setting the osteoid matrix which further densify and mineralize, bone remodeling process is not a fragmented sequence of events and, in fact osteoclasts and osteoprogenitors are intermingled on the eroded surfaces [47]. Therefore, our model may help to improve our understanding on osteoblasts behavior during such orchestrated process.

3.5. Mechanism of Sr^{2+}-driven physiological to pathological transition of bone components

Based on the present results, we propose a possible mechanism for the Sr^{2+}-driven structural destabilization of bone-like components in our model (Fig. 5g). The excess of Sr^{2+} in the mineralizing medium hinders the crystallization of bone-like apatite platelets leading to the formation of micrometric Sr^{2+}-rich amorphous calcium phosphate particles Sr(ACP) within the collagen scaffold. These non-biomimetic amorphous particles, in turn, disturb the collagen self-assembly both at the fibril and suprafibrillar scales found in bone, yielding weaker mechanical properties. Indeed, it is well-known that bone mineral platelets (nanometric dimension) decrease the distance between the molecules bringing a better cohesion to the bone material [48,49]. Conversely, it is possible that steric effects resulting from non-physiological microparticles preclude proper molecules/fibrils aggregation. Although Sr(ACP) was never reported *in vivo*, intracellular Sr^{2+}-rich ACP was previously
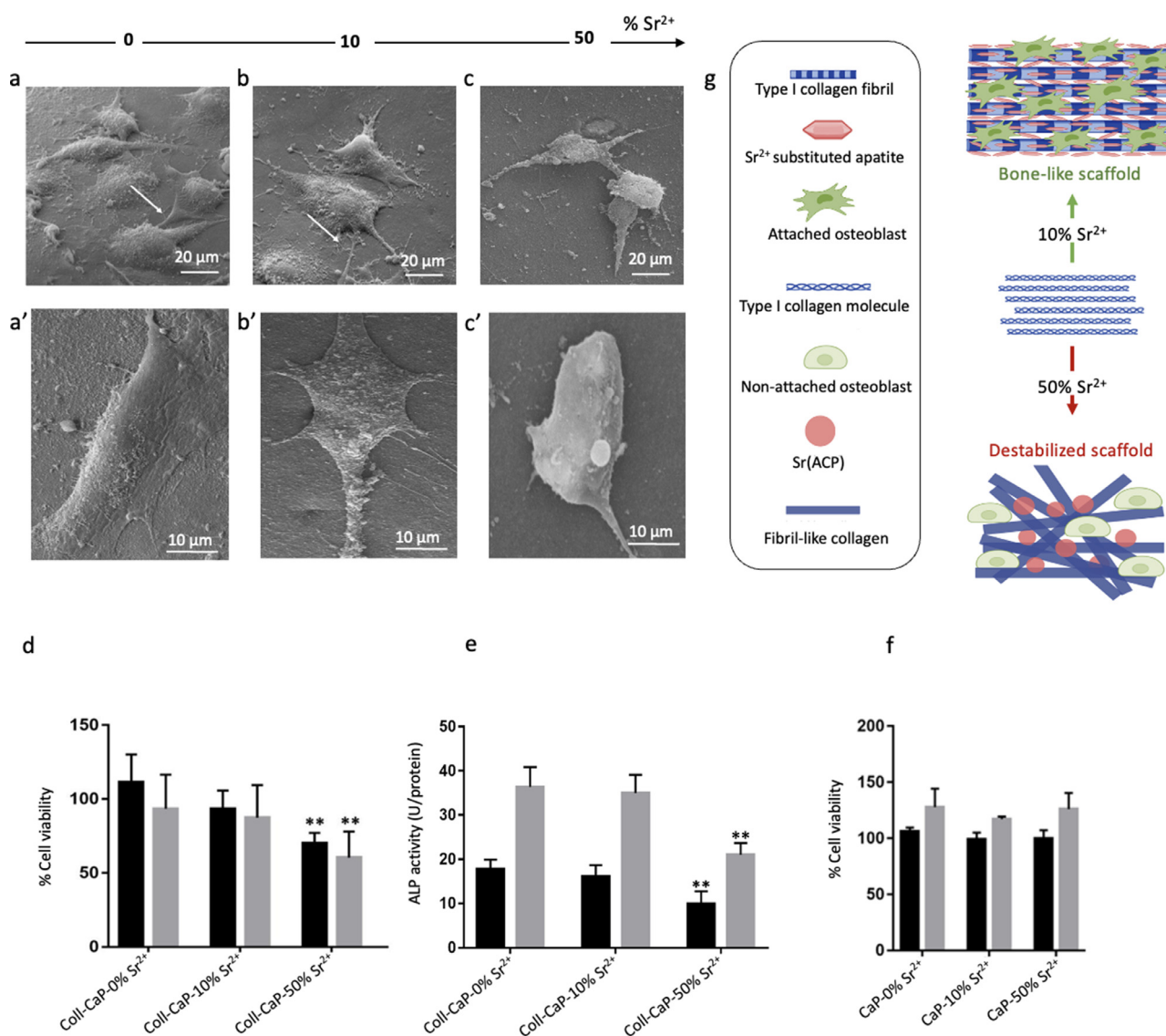
Fig. 5. MC3T3-E1 pre-osteoblastic cells grown on collagen scaffolds or in the presence of CaP particles. (a-c and a'-c') SEM images of MC3T3-E1 cells cultured for 7 days on Coll-CaP-0%Sr^{2+}, Coll-CaP-10%Sr^{2+} and Coll-CaP-50%Sr^{2+} scaffolds at two different magnifications. (d) % Cell viability versus control measured by MTT assay after 7 days (black bars) and 14 days (grey bars) of culture. (e) ALP activity of osteoblasts after 7 days (black bars) and14 days (grey bars) of culture. (f) MC3T3-E1 cells grown in the presence of CaP-0%Sr^{2+}, CaP-10%Sr^{2+}, and CaP-50%Sr^{2+} particles. % Cell viability versus control measured by MTT assay after 7 days (black bars) and 14 days (grey bars) of culture. Results represent the mean values $\pm$ standard deviation for triplicate determination for one experiment. Multiple statistical comparisons were performed by one-way ANOVA, ** $p < 0.01$. (g) Schematic of the dose-dependent effect of strontium on bone components. Illustration prepared with Biorender.com.

observed [50–52]. In addition, studies have shown that Sr^{2+} accumulates in the regions of new bone formation, more specifically near the mineralization front and in the region surrounding the osteoid, which may preclude bone maturation, as suggested by our model [12]. In our model, Sr^{2+} excess hinders the maturation of bone components, in agreement with the Sr^{2+}- driven skeletal disorders [6,21].

4. Conclusions

In summary, our *in vitro* biomimetic model shows that the structural hallmarks of bone tissue, namely collagen architecture, apatite structure, and cells activity, are destabilized at excess Sr^{2+}. Concomitantly, no obvious alterations are produced at a physiological-like concentration of Sr^{2+}. We propose that Sr(ACP) particles form within the scaffold at high doses of Sr^{2+}, disturbing the architecture of collagen fibrils and leading to a decrease

in the elasticity of the biomimetic scaffold. Along with *in vivo* observations, where a dose/effect relationship is observed for Sr^{2+}, these findings account for the Sr^{2+} concentration-driven switch from physiological to pathological of the main components of bone tissue and therefore the paradoxical impacts of this element on bone mineralization. The destabilization of collagen architecture by Sr(ACP) is particularly intriguing since amorphous calcium phosphate is described as a crucial precursor in bone mineralization. It is worth mentioning that some reports have speculated that bone disorders such as fibrogenesis imperfecta may be associated with a large amount of amorphous calcium phosphate, which in turn interferes with the assembly of collagen fibrils.[31,32]. Further investigation of the structure of organic and inorganic components in pathologic bone is needed to confirm whether the mechanism found in our model is also observed *in vivo*. From a broader standpoint, our results shed new light on how pathologies destabilize the extracellular matrix of bone, while the versatility of our

model opens perspectives for understanding the involvement of other ions and organic additives in bone mineralization in both physiological and pathological contexts.

Declaration of Competing Interests

The authors declare that they have no known competing financial interests or personal relationships that could have appeared to influence the work reported in this paper.

Supplementary materials

Supplementary material associated with this article can be found, in the online version, at doi:10.1016/j.actbio.2023.07.043.

References

[1] S. Pors Nielsen, The biological role of strontium, Bone 35 (2004) 583–588.
[2] E. Bonnelye, A. Chabadel, F. Saltel, P. Jurdic, Dual effect of strontium ranelate: Stimulation of osteoblast differentiation and inhibition of osteoclast formation and resorption in vitro, Bone 42 (2008) 129–138.
[3] T. Sozen, L. Ozisik, N.Calik Basaran, An overview and management of osteoporosis, Eur. J. Rheumatol. 4 (2017) 46–56.
[4] M. Pilmane, K. Salma-Ancane, D. Loca, J. Locs, L. Berzina-Cimdina, Strontium and strontium ranelate: historical review of some of their functions, Mater. Sci. Eng. C 78 (2017) 1222–1230.
[5] P.J. Marie, Strontium as therapy for osteoporosis, Curr. Opin. Pharmacol. 5 (2005) 633–636.
[6] P.C. D'Haese, I. Schrooten, W.G. Goodman, W.E. Cabrera, L.V. Lamberts, M.M. Elseviers, M.M. Couttenye, M.E. De Broe, Increased bone strontium levels in hemodialysis patients with osteomalacia, Kidney Int. 57 (2000) 1107–1114.
[7] I. Schrooten, M.M. Elseviers, L.V. Lamberts, M.E. De Broe, P.C. D'Haese, Increased serum strontium levels in dialysis patients: an epidemiological survey, Kidney Int. 56 (1999) 1879–1885.
[8] M.M. Couttenye, P.C. D'Haese, W.J. Verschoren, G.J. Behets, I. Schrooten, M.E. De Broe, Low bone turnover in patients with renal failure, Kidney Int. Suppl. 56 (1999) 70–76.
[9] M.R. Laurent, N. Bravenboer, N.M. Van Schoor, R. Bouillon, J.M. Pettifor, P. Lips, Rickets and osteomalacia, in: Primer on the Metabolic Bone Diseases and Disorders of Mineral Metabolism, 2018, pp. 684–694.
[10] B.O.Y. Frame, A.M. Parfitt, Osteomalacia : Current Concepts 25 (2017) 966–982.
[11] I. Anderson, A.E.R. Campbell, A. Dunn, J.B.M. Runciman, Osteomalacia in elderly women, Scott Med. J. 11 (1966) 429–435.
[12] C. Li, O. Paris, S. Siegel, P. Roschger, E.P. Paschalis, K. Klaushofer, P. Fratzl, Strontium is incorporated into mineral crystals only in newly formed bone during strontium ranelate treatment, J. Bone Mineral Res. 25 (2010) 968–975.
[13] S.G. Dahl, P. Allain, P.J. Marie, Y. Mauras, G. Boivin, P. Ammann, Y. Tsouderos, P.D. Delmas, C. Christiansen, Incorporation and distribution of strontium in bone, Bone 28 (2001) 446–453.
[14] A.L. Rossi, S. Moldovan, W. Querido, A. Rossi, J. Werckmann, O. Ersen, M. Farina, Effect of strontium ranelate on bone mineral: analysis of nanoscale compositional changes, Micron 56 (2014) 29–36.
[15] Z.Y. Li, W.M. Lam, C. Yang, B. Xu, G.X. Ni, S. a Abbah, K.M.C. Cheung, K.D.K. Luk, W.W. Lu, Chemical composition, crystal size and lattice structural changes after incorporation of strontium into biomimetic apatite, Biomaterials 28 (2007) 1452–1460.
[16] W. Querido, A.P.C. Campos, E.H. Martins Ferreira, R.A.S. San Gil, A.M. Rossi, M. Farina, Strontium ranelate changes the composition and crystal structure of the biological bone-like apatite produced in osteoblast cell cultures, Cell Tissue Res. 357 (2014) 793–801.
[17] C. Bussola Tovani, A. Gloter, T. Azaïs, M. Selmane, A.P. Ramos, N. Nassif, Formation of stable strontium-rich amorphous calcium phosphate: Possible effects on bone mineral, Acta Biomater. 92 (2019) 315–324.
[18] N. Reznikov, M. Bilton, L. Lari, M.M. Stevens, R. Kröger, Fractal-like hierarchical organization of bone begins at the nanoscale, Science (2018) 360.
[19] Y. Wang, T. Azaïs, M. Robin, A. Vallée, C. Catania, P. Legriel, G. Pehau-Arnaudet, F. Babonneau, M.M. Giraud-Guille, N. Nassif, The predominant role of collagen in the nucleation, growth, structure and orientation of bone apatite, Nat. Mater. 11 (2012) 724–733.
[20] L. Oste, A.R. Bervoets, G.J. Behets, G. Dams, R.L. Marijnissen, H. Geryl, L.V. Lamberts, S.C. Verberckmoes, V.O. Van Hoof, M.E. De Broe, P.C. D'Haese, Time-evolution and reversibility of strontium-induced osteomalacia in chronic renal failure rats, Kidney Int 67 (2005) 920–930.
[21] I. Schrooten, G.J.S. Behets, W.E. Cabrera, S.R. Vercauteren, L.V. Lamberts, S.C. Verberckmoes, A.J. Bervoets, G. Dams, W.G. Goodman, M.E. De Broe, P.C. D'Haese, Dose-dependent effects of strontium on bone of chronic renal failure rats, Kidney Int. 63 (2003) 927–935.
[22] E. Storey, Strontium "rickets": bone, calcium and strontium changes, Australas. Ann. Med. 10 (1961) 213–222.
[23] A. Akiva, M. Kerschnitzki, I. Pinkas, W. Wagermaier, K. Yaniv, P. Fratzl, L. Addadi, S. Weiner, Mineral formation in the larval zebra fish tail bone occurs via an acidic disordered calcium phosphate phase, J. Am. Chem. Soc 138 (2016) 14481–14487.
[24] J. Mahamid, A. Sharir, L. Addadi, S. Weiner, Amorphous calcium phosphate is a major component of the forming fin bones of zebrafish: Indications for an amorphous precursor phase, Proc. Natl. Acad. Sci. U. S. A. 105 (2008) 12748–12753.
[25] F. Gobeaux, E. Belamie, G. Mosser, P. Davidson, P. Panine, M.M. Giraud-Guille, Cooperative ordering of collagen triple helices in the dense state, Langmuir 23 (2007) 6411–6417.
[26] I. Bergman, R. Loxley, Two improved and simplified methods for the spectrophotometric determination of hydroxyproline, Anal. Chem. 35 (1963) 1961–1965.
[27] K.M. Nuss, J.A. Auer, A. Boos, B. von Rechenberg, An animal model in sheep for biocompatibility testing of biomaterials in cancellous bones, BMC Musculoskelet. Disord. 7 (2006) 67.
[28] T. Mosmann, Rapid colorimetric assay for cellular growth and survival: application to proliferation and cytotoxicity assays, J. Immunol. Methods 65 (1983) 55–63.
[29] Z. Ren, L.D. Do, G. Bechkoff, S. Mebarek, N. Keloglu, S. Ahamada, S. Meena, D. Magne, S. Pikula, Y. Wu, R. Buchet, Direct determination of phosphatase activity from physiological substrates in cells, PLoS One 10 (2015) e0120087.
[30] Y. Wang, S. Von Euw, G. Laurent, C. Crevant, L. Bonhomme-Coury, M.M. Giraud-Guille, F. Babonneau, N. Nassif, T. Azaïs, Impact of collagen confinement vs. ionic substitutions on the local disorder in bone and biomimetic apatites, Mater. Horiz. 1 (2014) 224–231.
[31] J.R. Ralphs, T.C.B. Stamp, P.J.C. Dopping-Hepenstal, S.Y. Ali, Ultrastructural features of the osteoid of patients with fibrogenesis imperfecta ossium, Bone 10 (1989) 243–249.
[32] H.A. Sissons, Fibrogenesis imperfecta ossium (Baker's disease): a case studied at autopsy, Bone 27 (2000) 865–873.
[33] M. Robin, C. Bussola Tovani, J.M. Krafft, G. Costentin, T. Azaïs, N. Nassif, The concentration of bone-related organic additives drives the pathway of apatite formation, Cryst. Growth Des. 21 (2021) 3994–4004.
[34] M. Quade, M. Schumacher, A. Bernhardt, A. Lode, M. Kampschulte, A. Voß, P. Simon, O. Uckermann, M. Kirsch, M. Gelinsky, Strontium-modification of porous scaffolds from mineralized collagen for potential use in bone defect therapy, Mater. Sci. Eng. C 84 (2018) 159–167.
[35] Z. Ye, Y. Qi, A. Zhang, B.J. Karels, C. Aparicio, Biomimetic mineralization of fibrillar collagen with strontium-doped hydroxyapatite, ACS Macro Lett. 12 (2023) 408–414.
[36] J. Silvent, M. Robin, C. Bussola Tovani, Y. Wang, F. Soncin, S. Delgado, T. Azaïs, C. Sassoye, M.-M. Giraud-Guille, J.-Y. Sire, N. Nassif, Collagen suprafibrillar confinement drives the activity of acidic calcium-binding polymers on apatite mineralization, Biomacromolecules 22 (2021) 2802–2814.
[37] M. Allen, D. Poggiali, K. Whitaker, T.R. Marshall, R.A. Kievit, Raincloud plots: A multi-platform tool for robust data visualization, Wellcome Open Res. 4 (2019).
[38] X. Zhu, J. Chen, L. Scheideler, R. Reichl, J. Geis-Gerstorfer, Effects of topography and composition of titanium surface oxides on osteoblast responses, Biomaterials 25 (2004) 4087–4103.
[39] M.K. Driscoll, X. Sun, C. Guven, J.T. Fourkas, W. Losert, Cellular contact guidance through dynamic sensing of nanotopography, ACS Nano 8 (2014) 3546–3555.
[40] C.J. Lowe, I.M. Reucroft, M.C. Grota, D.I. Shreiber, Production of highly aligned collagen scaffolds by freeze-drying of self-assembled, fibrillar collagen gels, ACS Biomater. Sci. Eng. 2 (2016) 643–651.
[41] U. Stachewicz, T. Qiao, S.C.F. Rawlinson, F.V. Almeida, W.Q. Li, M. Cattell, A.H. Barber, 3D imaging of cell interactions with electrospun PLGA nanofiber membranes for bone regeneration, Acta Biomater. 27 (2015) 88–100.
[42] A.A. Khalili, M.R. Ahmad, A Review of cell adhesion studies for biomedical and biological applications, Int. J. Mol. Sci. 16 (2015) 18149–18184.
[43] C.B. Tovani, T.M. Oliveira, M.P.R. Soares, N. Nassif, S.Y. Fukada, P. Ciancaglini, A. Gloter, A.P. Ramos, Strontium calcium phosphate nanotubes as bioinspired building blocks for bone regeneration, ACS Appl. Mater. Interfaces 12 (2020) 43422–43434.
[44] J.Q. Feng, E.L. Clinkenbeard, B. Yuan, K.E. White, M.K. Drezner, Osteocyte regulation of phosphate homeostasis and bone mineralization underlies the pathophysiology of the heritable disorders of rickets and osteomalacia, Bone 54 (2013) 213–221.
[45] A.B. Sedman, A.C. Alfrey, N.L. Miller, W.G. Goodman, Tissue and cellular basis for impaired bone formation in aluminum-related osteomalacia in the pig, J. Clinic. Investig. 79 (1987) 86–92.
[46] J. You, Y. Zhang, Y. Zhou, Strontium functionalized in biomaterials for bone tissue engineering: a prominent role in osteoimmunomodulation, Front Bioeng Biotechnol 10 (2022).

[47] J.-M. Delaisse, T.L. Andersen, H.B. Kristensen, P.R. Jensen, C.M. Andreasen, K. Søe, Re-thinking the bone remodeling cycle mechanism and the origin of bone loss, Bone 141 (2020) 115628.

[48] P. Fratzl, N. Fratzl-Zelman, K. Klaushofer, Collagen packing and mineralization. An x-ray scattering investigation of turkey leg tendon, Biophys. J. 64 (1993) 260–266.

[49] N. Nassif, F. Gobeaux, J. Seto, E. Belamie, P. Davidson, P. Panine, G. Mosser, P. Fratzl, M.-M.Giraud Guille, Self-assembled collagen–apatite matrix with bone-like hierarchy, Chem. Mater. 22 (2010) 3307–3309.

[50] S.C. Skoryna, Effects of oral supplementation with stable strontium, Can. Med. Assoc. J. 125 (1981) 703–712.

[51] A.P. Somlyo, A.V. Somlyo, C.E. Devine, P.D. Peters, T.A. Hall, Electron microscopy and electron probe analysis of mitochondrial cation accumulation in smooth muscle, J. Cell Biol. 61 (1974) 723–742.

[52] L.D. Peachey, Electron microscopic observations on the accumulation of divalent cations in intramitochondrial granules, J. Cell Biol. 20 (1964) 95–111.